

Giant pyroelectric effect for energy conversion via tuning lattice compatibility

Chenbo Zhang,^{1,2} Zhuohui Zeng,¹ Zeyuan Zhu,¹ Nobumichi Tamura,³ Xian Chen^{1*}

¹Mechanical and Aerospace Engineering, Hong Kong University of Science and Technology, Hong Kong

²Institute for Advanced Study, Hong Kong University of Science and Technology, Hong Kong

³Advanced Light Source, Lawrence Berkeley National Laboratory, CA 94720, USA

*E-mail: xianchen@ust.hk

Abstract

Searching for performant pyroelectric materials is gathering research interest for its potential in clean electricity generation and waste heat harvesting. Here we report achieving the giant pyroelectric effect in materials undergoing a first-order phase transformation with high reversibility by tuning the crystallographic compatibility. The single crystalline $\text{Ba}_{0.95}\text{Ca}_{0.05}\text{Ti}_{0.99}\text{Zr}_{0.005}\text{Ce}_{0.005}\text{O}_3$ shows a pyroelectric coefficient of $1.93 \mu\text{C}/(\text{cm}^2\text{K})$, substantially higher than that of most of the state-of-the-art pyroelectric generators by orders of magnitude. We demonstrate that it lights a LED directly without attaching an external power source and consistently generates about $6 \mu\text{A}/\text{cm}^2$ current density by small thermal fluctuations near 100°C over 540 complete phase transformation cycles with no degradation. This promising material candidate brings pyroelectric energy conversion closer to a practical realization.

Electrically polarized crystals naturally exhibit the pyroelectric effect: a change in temperature causes a change in its spontaneous electrical polarization. The earliest documented observation of pyroelectric effect in stones such as tourmaline can date back to ancient Greece. [1] Since the 1960s, pyroelectric materials have attracted profound attention due to their suitability for thermal sensing and thermal imaging [2, 3]. Later, some theoretical models were proposed by Olsen, Evans and Drummond to explore the heat-to-electricity conversion as utilizing these materials as the dielectric layer in capacitors, called dielectric power converter (DPC) [4–6]. Their work underlies the thermodynamics of energy conversion by pyroelectric effect. This idea was further optimized and demonstrated in relaxor ferroelectrics. [7, 8] As the nano-fabrication techniques flourished, pyroelectric energy conversion designs based on Olsen cycles have been revitalized in thin film devices. [9–12] One of the obstacles preventing pyroelectric energy conversion from broad commercialization is that the pyroelectric effect is weak in common relaxor thin

films, e.g. $0.055 \mu\text{C}/(\text{cm}^2 \text{ K})$ in PMN–0.32PT at room temperature [12]. Several attempts, such as actively sweeping the bias electric field between two values far apart [6, 12], have been made to circumvent this weakness. Without connection to external bias field, the pyroelectric current generation becomes rather marginal, only at several nano ampere scale. [10–14] Recent advances in innovative thermal management [12, 15] and exquisite nano-devices [10, 13, 14] have pushed the device performance towards its current limit. This field urgently calls for new materials to intrinsically improve the multiferroic-thermal response.

Core material development strategies

Pyroelectric effect is characterized by the pyroelectric coefficient defined as dP/dT , where P is the polarization and T is the temperature. The foremost task of material development for pyroelectric energy conversion is to search for a material having a large pyroelectric coefficient. In the temperature vicinity of a phase transformation, dP/dT could potentially reach its maximum value. For example, the pyroelectric coefficient of single crystal BaTiO_3 during its first-order phase transformation is $\frac{\Delta P_r}{\Delta T} \approx 1 \mu\text{C}/\text{cm}^2\text{K}$, as calculated from experimental measurements [16]. That is about twice of the highest dP/dT reported in lead-based relaxor PMN-0.32PT single crystal along [111] polar axis at 180°C [17], and 20 times larger than relaxor ferroelectric thin films[12]. Utilizing this fact, people has indeed demonstrated promising energy conversion performance using single crystal BaTiO_3 by a small temperature fluctuation near the first-order phase transformation. [18] Reserved energies stored as small thermal fluctuations are abundant and rapidly growing in nature and from human activities. These rich thermal energies are mainly around 100°C . Hence, finding the ferroelectric material undergoing first-order phase transformation at a proper temperature with a giant pyroelectric coefficient is a core strategy of material development.

From energetic analysis, the cost of pyroelectric energy conversion is the heat in the heating half cycle or the work required to cool the active material in the cooling half cycle, while the return is the change of polarization stored as the electrostatic energy. The ratio $(1/c)(dP/dT)$ where c is the heat capacity at a fixed bias field, is a natural choice of figure of merit, which is in fact equivalent to one of the proposed figures of merit in this research field. [19, 20] Across a phase transformation, the effective heat capacity integrated over temperature is the latent heat ℓ , while the integrated dP/dT is the jump of polarization $\llbracket P \rrbracket$. Based on thermodynamic analysis of a new energy conversion design without application of a bias field [21], a new figure of merit was proposed to consider the conversion in a temperature range covering a complete loop of phase transformation. That is,

$$\text{FOM} = \frac{\kappa \llbracket P \rrbracket}{\ell}, \quad (1)$$

where κ is the maximum value of $|dP/dT|$ near the transformation temperature, $\llbracket P \rrbracket$ is the jump of polarization across the phase transformation corresponding to the latent heat ℓ . Eq. (1) rationalizes the searching of ferroelectric materials specially desirable for conversion from small temperature fluctuations to electricity by phase transformation. It is one of the key factors considered in this paper for material development.

Lattice compatibility is an unprecedented factor that determines the thermal hysteresis and reversibility of structural phase transformation in crystalline solids.[22, 23] The primary condition of compatibility is $\lambda_2 = 1$ where λ_2 is the middle principle stretch of the transformation tensor.[23] The value of λ_2 can be tuned by the lattice parameters of initial and final phases, used as a search index for low-hysteresis shape memory alloys [24–27] and transforming oxides with enhanced structural reversibility [28–31]. Some recent discoveries have shown that ferroic properties such as electromagnetic property [32], ferroelectric property [31] and elasto/magneto caloric property [33] are closely related to the lattice compatibility, and can be optimized when lattice parameters meet the $\lambda_2 = 1$ condition. Since ferroic properties are keenly sensitive to crystal structures, the crystallographic compatibility is another important design factor for developing a transforming material with small thermal hysteresis and stable pyroelectric functionality throughout numerous phase transformations.

Considering all aforementioned factors for material development, we select three dopants Ca, Zr, Ce to develop Barium Titanate based ferroelectrics, named as tridoped BT. We fixed Ca addition at 5 at.% to ensure a reversible tetragonal (ferroelectric) to cubic (paraelectric) transformation below 120°C [34, 35]. Addition of Zr increases the polarization jump across the phase transformation.[21, 31] Slightly doping Ce to lead-free Barium Titanate system has shown prominent leakage prevention in experiments.[36] Tuning compositions of the dopants Zr and Ce within the range of 0.1 at.% \sim 1 at.% slightly adjusts the lattice parameters to satisfy the compatibility condition $\lambda_2 = 1$. A series of $\text{Ba}_{0.95}\text{Ca}_{0.05}\text{Ti}_{1-x-y}\text{Zr}_x\text{Ce}_y\text{O}_3$ oxides were synthesized by solid-state reaction and densification process to obtain homogeneous polycrystalline rods of high density (Methods). Fig. 1 (a) and (b) show the temperature dependent spontaneous polarization and corresponding $|dP/dT|$ of five compositions, labeled as “Zr $_x$ Ce $_y$ ” for $(x, y) = (0.005, 0.005), (0.001, 0.005), (0.01, 0.005), (0.01, 0.01)$ and $(0.01, 0.001)$. Their chemical homogeneity were examined by Energy-dispersive X-ray Spectroscopy (EDS) analysis. The variation of doping elements Ca, Zr and Ce is sufficiently small with respect to their mean values (Fig. S4). All of the tridoped BT show large $\llbracket P \rrbracket$ and steep dP/dT slope within 100 to 120°C, among which the Zr $_{0.005}$ Ce $_{0.005}$ specimen gives the largest $\llbracket P \rrbracket = 7.58\mu\text{C}/\text{cm}^2$ and $\kappa = 1.31\mu\text{C}/\text{cm}^2\text{K}$. The thermal analysis by DSC in Fig. 1(c) reaffirms that they all undergo first-order phase transformations as big peaks of the heat flow are detected during heating and cooling through the transformation temperatures. Table 1 summarizes

the pyroelectric properties and FOM defined in Eq. 1 for these five samples compared with typical ferroelectric poly/single crystals reported in literature. Among them, Zr_{0.005} Ce_{0.005} gives the largest FOM, that is 1.52 $\mu\text{C}^2/\text{JcmK}$ in polycrystal and 3.55 $\mu\text{C}^2/\text{JcmK}$ in single crystal.

Correlation between pyroelectric properties and lattice compatibility

The lattice parameters were measured by neutron diffraction at the general purpose powder diffractometer beamline (GPPD) at China Spallation Neutron Source, suitable for structural characterization of large bulk samples.[37] We conducted the temperature varying diffraction experiments for densified polycrystalline rods ($\phi 5 \times 50\text{mm}^3$) from 40°C to 140°C (Methods). The tetragonality defined as the c/a ratio is presented in Fig. 1(d) where the lattice parameters were refined based on the diffraction patterns at different temperatures (Fig. S5 and Table S1). Stark discontinuity of tetragonality exists in all compositions, which evidences the first-order structural phase transformation in consistent with the abrupt jump of polarization (Fig. 1(a)), the singularity of pyroelectric coefficient (Fig. 1(b)) and the big heat flow peaks in DSC measurements (Fig. 1(c)).

The composition Zr_{0.005} Ce_{0.005} shows the smallest thermal hysteresis and largest FOM among all tested compositions in Fig. 1(e) and (f), meanwhile it satisfies closely the compatibility condition as indicated in Fig. 1(g). (See Supplementary information for the calculation of compatibility condition.) It has been theorized that the thermal hysteresis and reversibility of a solid phase transformation strongly relies on the compatibility condition.[26] Our observation in pyroelectric material development implies a correlation between $\lambda_2 = 1$ and the abrupt change in the spontaneous polarization and the singular pyroelectric coefficient across the first-order phase transformation, which resonates with the minimization of hysteresis in Fig. 1(f). The large FOM given by the composition Zr_{0.005} Ce_{0.005} makes it an ideal material candidate for a pyroelectric energy conversion demonstration.

Improved pyroelectric effect in coarse-grained polycrystals and single crystals

For demonstration, it is critical to fabricate a high quality capacitor with the capacitance sensitive to temperature variation within the thermal fluctuation range. A previous energy conversion attempt [18] by first-order phase transformation evidently suggests that the single BaTiO₃ crystal can magnificently enhance the performance of the device. We adopted the floating zone method (Methods), an economic way to grow single crystals, to coarsen the grains in two fine-grained polycrystals: Zr_{0.01} Ce_{0.001} and Zr_{0.005} Ce_{0.005}. We aimed to synthesize single or coarse-grained crystals used for energy conversion device. The as-grown crystal rod was sliced along its growth direction. After mechanical polishing,

both Zr_{0.01}Ce_{0.001} and Zr_{0.005}Ce_{0.005} slices are semi-transparent in Fig. 2. Since we used polycrystal seeds for the floating zone process, the cutting process of the as-grown rod was done without acknowledgment of orientation information. Fig. 2 shows the post-cut orientation maps characterized by synchrotron X-ray Laue microdiffraction at Advanced Light Source, Beamline 12.3.2 at Lawrence Berkeley National Lab. Clearly, the Zr_{0.005}Ce_{0.005} plate is a single crystal of millimeter size, while the Zr_{0.01}Ce_{0.001} plate is a coarse-grained crystal having multiple millimeter grains. The surface normal of Zr_{0.005}Ce_{0.005} is measured as [0.9, 1.5, 1.8] written in the crystal basis. Although it is not perfectly aligned with the polar axis [001], its $\llbracket P \rrbracket$ reaches $11.7 \mu\text{C}/\text{cm}^2$, corresponding to $\kappa = 1.93 \mu\text{C}/\text{cm}^2\text{K}$, shown in Fig. 3(a)-(b). These values are even larger than the reported values of single crystal BaTiO₃ aligned with its polar axis [16]. In supplementary information, we show that similar pyroelectric behaviors are observed in a Zr_{0.005}Ce_{0.005} slice from another rod grown by the same synthesis procedure. Table 1 compares the pyroelectric properties among important relaxor ferroelectrics in literature. Since the goal of energy conversion is to harvest low-grade waste heat, we consider 20°C temperature difference near 100°C to benchmark the ferroelectrics in our work and literature. Zr_{0.005}Ce_{0.005} single crystal exhibits by far the largest polarization jump and pyroelectric coefficient. The coarsened Zr_{0.01}Ce_{0.001} crystal also exhibits some degree of improvement in $\llbracket P \rrbracket$ compared with its fine-grained polycrystal counterpart.

Energy conversion demonstration for long thermal cycles

We make planar capacitors using the Zr_{0.005}Ce_{0.005} single crystal and the Zr_{0.01}Ce_{0.001} coarse-grained slices (see Methods for detailed geometry). The demonstration apparatus is illustrated in Fig. 4(a)-(b), which was analyzed by a thermodynamic model with complete removal of external bias field during energy conversion [21, 38]. A non-transforming capacitor used as charge reservoir is connected to the phase-transforming capacitor. Both are grounded and bridged via a resistor to measure the electric signal generated by first-order phase transformation of the active material. The apparatus parameters are given in Methods. The capacitors were initially charged up to hold sufficient initial charges, then detached from the external power source throughout the heating and cooling cycles. Those charges flow back and forth between the transforming and non-transforming capacitors driven by the ferro-to-paraelectric phase transformation. We measured the electric voltage on the load resistor R in Fig. 4(b) to calculate the pyroelectric current, in short pyro-current. Note that the voltage signal can be magnified by using a large resistor, but it does not represent a true improvement of pyroelectric energy conversion performance, as the load resistance is given in practical applications. Hence, pyro-current is a more proper meter for

pyroelectric energy conversion in current setup.

Fig. 4(c) demonstrates continuous generation of electricity more than 3 hours by Zr_{0.005} Ce_{0.005} capacitor, compared to the Zr_{0.01} Ce_{0.001} capacitor over hundreds of transformation cycles. The pyro-current generated by the Zr_{0.005} Ce_{0.005} single crystal capacitor reaches up to 1 μA stably and continuously lasting over 500 transformation cycles. For the Zr_{0.01} Ce_{0.001} coarse-grained capacitor, the pyro-current generated in the first few cycles is 0.5 μA . In order to benchmark capacitors with different area, we calculated the current density, i.e. current per area: 6 $\mu\text{A}/\text{cm}^2$ for Zr_{0.005} Ce_{0.005} and 2 $\mu\text{A}/\text{cm}^2$ for Zr_{0.01} Ce_{0.001}. These results are aligned with our theoretical prediction by figure of merit for material development. In addition, the Zr_{0.01} Ce_{0.001} coarse-grained capacitor suffers pyro-current degradation due to leakage [38] over a long term of energy conversion process. The half-life – number of cycles since a full recharge till the peak signal reduces 50% – shortens considerably after each full recharge. It requires 4 full recharges to maintain a decent power output at the 106th cycle, labeled in the bottom panel of Fig. 4(c). In contrast, the Zr_{0.005} Ce_{0.005} capacitor has no visible electric degradation during the first 135 cycles. After a recharge, the generation of pyro-current sustains for 365 cycles until the second recharge, corresponding to the top panel of Fig. 4 (c). An important observation is that the number of cycles in each half-life in the Zr_{0.01} Ce_{0.001} capacitor keeps shrinking, which implies a functional degradation of the transforming material. The Zr_{0.005} Ce_{0.005} capacitor with λ_2 much closer to 1 exhibits magnificent reversibility for cyclic phase transformation. The thermal reversibility of these two capacitors were examined by cyclic DSC experiments, shown in Fig. 4(d). The Zr_{0.005} Ce_{0.005} capacitor after 1024 thermal cycles shows no migration of transformation temperature (115°C) and no magnification of the hysteresis (2.7°C). This coincides with the satisfaction of the compatibility condition $\lambda_2 = 1$ (Fig. 1(f)-(g)). Thanks to the phase stability, low hysteresis and large pyro-current generated per cycle, the Zr_{0.005} Ce_{0.005} capacitor can directly light up a LED during both heating (Fig. 4b) and cooling process through phase transformation (see Movie S1). We then cut 38 pieces of the similar sizes from several rods of Zr_{0.005} Ce_{0.005} synthesized by the same method, and assembled them in parallel in our demonstration setup, which generates stably 15 μA electric current in consecutive cycles (Fig. S4).

Enabling pyroelectric energy conversion for the broad society is an inter-disciplinary and multifaceted grand challenge. Core material development is undoubtedly one of the key imperatives. Tuning lattice parameters to satisfy lattice compatibility criteria is a powerful strategy of searching for materials with minimal functional degradation and abrupt ferroic property change across the phase transformation. Although aspects like manageable temperature cycling, efficient heat transfer, collecting intermittent electricity and compact device packaging still call for breakthrough improvement, this work is a substantial step from the aspect of material development towards the practical realization of pyroelectric energy

conversion.

Author contributions

X. C. designed and supervised the research; C. Z. performed ferroelectric characterization, demonstrated the energy conversion via a self-designed apparatus; C. Z. and Z. Zhu synthesized the specimens, and performed neutron diffraction experiments at CSNS; Z. Zeng and Z. Zhu conducted DSC measurements; N. T. performed synchrotron X-ray Laue microdiffraction experiments and analyzed the data; X. C. wrote the manuscript; All authors agreed on the final version of manuscript.

Conflict of interests

The authors declare no conflict of interests.

Acknowledgments

The authors appreciate fruitful discussion with Dr. Yintao Song during the preparation of the manuscript. Lunhua He and Sihao Deng are acknowledged for their help on the neutron powder diffraction experiments which were performed at GPPD of the China Spallation Neutron Source (CSNS), Dongguan, China. C. Z., Z. Zeng, Z. Zhu and X. C. are grateful for financial support under GRF grants 16201118 and 16201019, CRF grant C6016-20G from the HK Research Grants Council and the Bridge Gap Fund, BGF.009.19/20, from the HKUST Technology Transfer Center. This research used BL12.3.2 which is a resource of the Advanced Light Source, a U.S. DOE Office of Science User Facility under contract no. DE-AC02-05CH11231.

References

- [1] Lang, S. B. Pyroelectricity: A 2300-year history. *Ferroelectrics* **7**, 231–234 (1974).
- [2] Whatmore, R. Pyroelectric devices and materials. *Rep. Prog. Phys.* **49**, 1335 (1986).
- [3] Bauer, S. & Ploss, B. A simple technique to interface pyroelectric materials with silicon substrates for infrared detection. *Ferroelectrics Letters Section* **9**, 155–160 (1989).

- [4] Drummond, J., Fargo, V., Ream, J., Briscoe, J. & Brown, D. Experimental demonstration of heat-to-electricity conversion within a dielectric. In *14th Intersociety Energy Conversion Engineering Conference*, vol. 2, 1819–1824 (1979).
- [5] Olsen, R. B. & Evans, D. Pyroelectric energy conversion: hysteresis loss and temperature sensitivity of a ferroelectric material. *J. Appl. Phys.* **54**, 5941–5944 (1983).
- [6] Olsen, R. B., Bruno, D. A. & Briscoe, J. M. Pyroelectric conversion cycles. *J. Appl. Phys.* **58**, 4709–4716 (1985).
- [7] Sebald, G., Pruvost, S. & Guyomar, D. Energy harvesting based on ericsson pyroelectric cycles in a relaxor ferroelectric ceramic. *Smart Mater. Struct.* **17**, 015012 (2008).
- [8] Sebald, G., Guyomar, D. & Agbossou, A. On thermoelectric and pyroelectric energy harvesting. *Smart Mater. Struct.* **18**, 125006 (2009).
- [9] Navid, A. & Pilon, L. Pyroelectric energy harvesting using Olsen cycles in purified and porous poly (vinylidene fluoride-trifluoroethylene)[P (VDF-TrFE)] thin films. *Smart Mater. Struct.* **20**, 025012 (2011).
- [10] Yang, Y., Wang, S., Zhang, Y. & Wang, Z. L. Pyroelectric nanogenerators for driving wireless sensors. *Nano Lett.* **12**, 6408–6413 (2012).
- [11] Bhatia, B., Damodaran, A. R., Cho, H., Martin, L. W. & King, W. P. High-frequency thermal-electrical cycles for pyroelectric energy conversion. *J. Appl. Phys.* **116**, 194509 (2014).
- [12] Pandya, S. *et al.* Pyroelectric energy conversion with large energy and power density in relaxor ferroelectric thin films. *Nat. Mater.* **17**, 432–438 (2018).
- [13] Ji, Y., Zhang, K., Wang, Z. L. & Yang, Y. Piezo–pyro–photoelectric effects induced coupling enhancement of charge quantity in BaTiO₃ materials for simultaneously scavenging light and vibration energies. *Energy Environ. Sci.* **12**, 1231–1240 (2019).
- [14] Sharma, A. P. *et al.* Lead-free relaxor-ferroelectric thin films for energy harvesting from low-grade waste-heat. *Scientific Reports* **11**, 1–10 (2021).
- [15] Pandya, S. *et al.* Direct measurement of pyroelectric and electrocaloric effects in thin films. *Phys. Rev. Applied* **7**, 034025 (2017).

- [16] Moya, X. *et al.* Giant electrocaloric strength in single-crystal BaTiO₃. *Adv. Mater.* **25**, 1360–1365 (2013).
- [17] Kumar, P., Sharma, S., Thakur, O., Prakash, C. & Goel, T. Dielectric, piezoelectric and pyroelectric properties of PMN–PT (68: 32) system. *Ceramics International* **30**, 585–589 (2004).
- [18] Bucsek, A., Nunn, W., Jalan, B. & James, R. D. Direct conversion of heat to electricity using first-order phase transformations in ferroelectrics. *Phys. Rev. Applied* **12**, 034043 (2019).
- [19] Lang, S. B. & Das-Gupta, D. K. Pyroelectricity: Fundamentals and applications. In *Handbook of advanced electronic and photonic materials and devices*, 1–55 (Elsevier, 2001).
- [20] Bowen, C. R. *et al.* Pyroelectric materials and devices for energy harvesting applications. *Energy Environ. Sci.* **7**, 3836–3856 (2014).
- [21] Zhang, C. *et al.* Power-source-free analysis of pyroelectric energy conversion. *Phys. Rev. Applied* **12**, 014063 (2019).
- [22] Ball, J. M. & James, R. D. Fine phase mixtures as minimizers of energy. *Arch. Ration. Mech. Anal.* **100**, 13 (1987).
- [23] Chen, X., Srivastava, V., Dabade, V. & James, R. D. Study of the cofactor conditions: conditions of supercompatibility between phases. *J. Mech. Phys. Solids* **61**, 2566–2587 (2013).
- [24] Cui, J. *et al.* Combinatorial search of thermoelastic shape-memory alloys with extremely small hysteresis width. *Nat. Mater.* **5**, 286–290 (2006).
- [25] Zarnetta, R. *et al.* Identification of quaternary shape memory alloys with near-zero thermal hysteresis and unprecedented functional stability. *Adv. Funct. Mater.* **20**, 1917–1923 (2010).
- [26] Song, Y., Chen, X., Dabade, V., Shield, T. W. & James, R. D. Enhanced reversibility and unusual microstructure of a phase-transforming material. *Nature* **502**, 85–88 (2013).
- [27] Chluba, C. *et al.* Ultralow-fatigue shape memory alloy films. *Science* **348**, 1004–1007 (2015).
- [28] Pang, E. L., McCandler, C. A. & Schuh, C. A. Reduced cracking in polycrystalline ZrO₂-CeO₂ shape-memory ceramics by meeting the cofactor conditions. *Acta Mater.* **177**, 230–239 (2019).
- [29] Jetter, J. *et al.* Tuning crystallographic compatibility to enhance shape memory in ceramics. *Phys. Rev. Materials* **3**, 093603 (2019).

- [30] Liang, Y. *et al.* Tuning the hysteresis of a metal-insulator transition via lattice compatibility. *Nat. Comm.* **11**, 1–8 (2020).
- [31] Wegner, M., Gu, H., James, R. D. & Quandt, E. Correlation between phase compatibility and efficient energy conversion in Zr-doped Barium Titanate. *Sci. Rep.* **10**, 1–8 (2020).
- [32] El-Khatib, S., Bhatti, K. P., Srivastava, V., James, R. & Leighton, C. Nanoscale magnetic phase competition throughout the $\text{Ni}_{50-x}\text{Co}_x\text{Mn}_{40}\text{Sn}_{10}$ phase diagram: Insights from small-angle neutron scattering. *Phys. Rev. Materials* **3**, 104413 (2019).
- [33] Zhao, D. *et al.* Giant caloric effect of low-hysteresis metamagnetic shape memory alloys with exceptional cyclic functionality. *Acta Mater.* **133**, 217–223 (2017).
- [34] Liu, X. *et al.* Ferroelectric, dielectric and pyroelectric properties of Sr and Sn codoped BCZT lead free ceramics. *Advances in Applied Ceramics* **114**, 436–441 (2015).
- [35] Coondoo, I. *et al.* Temperature-dependent Raman spectroscopy, domain morphology and photoluminescence studies in lead-free BCZT ceramic. *Ceramics International* **47**, 2828–2838 (2021).
- [36] Wang, S. *et al.* Influence of Ce doping on leakage current in $\text{Ba}_{0.5}\text{Sr}_{0.5}\text{TiO}_3$ films. *J. Phys. D: Appl. Phys.* **38**, 2253 (2005).
- [37] Chen, J. *et al.* The general purpose powder diffractometer at CSNS. *Physica B: Condensed Matter* **551**, 370–372 (2018).
- [38] Zhang, C. *et al.* Impact of leakage for electricity generation by pyroelectric converter. *Phys. Rev. Applied* **14**, 064079 (2020).
- [39] Balbashov, A. M. & Egorov, S. K. Apparatus for growth of single crystals of oxide compounds by floating zone melting with radiation heating. *Journal of Crystal Growth* **52**, 498–504 (1981).
- [40] Kimura, S. & Kitamura, K. Floating zone crystal growth and phase equilibria: A review. *Journal of the American Ceramic Society* **75**, 1440–1446 (1992).
- [41] Toby, B. H. EXPGUI, a graphical user interface for GSAS. *Journal of Applied Crystallography* **34**, 210–213 (2001).
- [42] Tamura, N. XMAS: A versatile tool for analyzing synchrotron X-ray microdiffraction data. In *Strain and dislocation gradients from diffraction: Spatially-Resolved Local Structure and Defects*, 125–155 (World Scientific, 2014).

Methods

Synthesis of Ca, Zr, Ce doped BaTiO₃ by floating zone method

The powders of CaCO₃(Alfa Aesar, 99.5%), CeO₂(Alfa Aesar, 99.9%), ZrO₂(Sigma Aldrich, 99%), BaCO₃(Alfa Aesar, 99.8%) and TiO₂(Alfa Aesar, 99.8%) were weighed and well mixed according to the stoichiometric formulation Ba_{0.95}Ca_{0.05}Ti_{1-x-y}Zr_xCe_yO₃, for $(x,y) = (0.001, 0.005), (0.005, 0.005), (0.01, 0.005), (0.01, 0.01),$ and $(0.01, 0.001)$. Then, the powder mixture was dissolved in the ethanol solvent, which was milled by zirconia balls in a planetary ball miller at 630rpm for 24hrs. The ball-milled solution was dried and calcined at 1000°C for 10 hours to obtain the tridoped Barium Titanate powder through solid state reaction. Under a 30MPa hydrostatic pressure at room temperature, the powder was hot-pressed for 30 minutes to form a rod-shape green body with size 10mm \times ϕ 6mm, in Figure S1(a) (Supplementary information). The sintering process is divided into two steps by four-mirror Infrared furnace (Quantum Design IRF11-001-00): 1) densification of feed and seed rods [38]; 2) grain-coarsening by floating-zone method [39, 40]. The densification was conducted as a pre-sintering process by passing through the focal point of the four mirrors slowly with the axial speed 3mm/hr and the angular speed 3rpm, in Figure S1 (b). Figure S1(c) shows the pre-sintered rod that is straighter and more homogeneous in shape compared to the conventionally sintered rod under high-temperature furnace. With much less sintering time, all pre-sintered rods show high densities ($5.4 \sim 5.6\text{g/cm}^3$) that is $> 90\%$ of theoretical density of BaTiO₃. We selected two densified rods as the seed and feed aligned vertically for the crystal growth by floating zone method at a growth speed 10mm/hr and relative angular speed 25rpm at an increasing lamp power. The molten zone in Figure S2(a) (Supplementary information) was created and monitored throughout the entire growth period. Finally, the as-grown rod was solidified as the furnace cools down. The rod was sliced along the growth direction as shown in Figure S2(b), followed by mechanical polish. The size of the ceramic slices is about $19.5 \times 5.5 \times 0.4 \text{ mm}^3$. The compositions of tridoped BT samples are characterized by the Energy-dispersive X-ray Spectroscopy analysis by JEOL 6390. Fig. S3 (Supplementary information) shows the normalized intensity of element Ba, Ti, O, Ca, Zr and Ce along a 1.2 mm line on surface for Zr0.01 Ce0.001 and Zr0.005 Ce0.005 samples. The atomic weight percentages were analyzed based by the spectra of the polycrystalline tridoped BT samples. The compositions are consistent with the nominal compositions. The temperature dependent ferroic properties were characterized by the aix ACCT TF2000E ferroelectric analyzer for both polycrystal bulk and coarsened grains floating zone samples at a temperature step 0.5°C.

The energy conversion demonstration was conducted by using the apparatus in Fig. 4(b). We use a non-transforming capacitor with capacitance 10 μ F and a 1 M Ω load resistor connected to the transform-

ing capacitor in series. The dimensions of the transforming capacitors are $16.5\text{mm}^2 \times 0.46\text{mm}$ for Zr_{0.005} Ce_{0.005} single crystal capacitor and $25.28\text{mm}^2 \times 0.44\text{mm}$ for Zr_{0.01} Ce_{0.001} coarse-grain capacitor. The pyroelectric current (i.e. pyro-current) was characterized as V/R where voltage V on the load resistor was measured by Agilent 34970A data acquisition module. Before energy conversion, the capacitors are electrically poled to achieve electric balance with the reference capacitor. The initial electric field in both transforming capacitors is 2kV/cm. Then the external charger was disconnected throughout whole energy conversion cycles under thermal cycles between 90 and 130°C. This setup was also used to light up the LED bulb solely by the Zr_{0.005} Ce_{0.005} capacitor. In the second demonstration, we cut 38 thin slices from several as-grown rods of composition Zr_{0.005} Ce_{0.005} synthesized by the same method, by which we made a grid of capacitors connected in parallel to demonstrate the power generation by thermal fluctuations. The total area of them is 2344.88mm², and the mean thickness is about 0.4mm. In this setting, we used a bigger reference capacitor (140μF) connected to the same load resistor. All capacitors were initially charged up to have 1.2 kV/cm electric field inside, then completely disconnect to the external power to begin the energy conversion cycles between 40 and 120°C. The generated pyro-current is given in Fig.S4 (Supplementary information).

Thermal analysis by differential scanning calorimetry (DSC)

The thermal analysis was conducted by differential scanning calorimetry (DSC) using TA Instruments DSC-250. The sample slice was polished on both sides in room temperature for good conduction. All polycrystalline tridoped BT samples were measured three complete thermal cycles at a heating/cooling rate of 5°C/min in the range from 40°C to 160°C in Fig.1(c). The transformation temperature was determined as the onsets of emission/absorption thermal peaks, labeled as the austenite start/finish A_s/A_f and martensite start/finish M_s/M_f temperatures. The thermal hysteresis was calculated as $\Delta T = (A_s + A_f - M_s - M_f)/2$. To reveal the thermal degradation, we performed 1024 thermal cycles on Zr_{0.005} Ce_{0.005} sample and 64 thermal cycles on Zr_{0.01} Ce_{0.001} sample at an accelerated rate of 10°C/min within a zoomed temperature range from 80°C and 130°C.

Structural characterization

The temperature dependent structural parameters were characterized by neutron diffraction at General Purpose Powder Diffractometer beamline (GPPD) at the China Spallation Neutron Source (CSNS). As an example, Fig. S5 (Supplementary information) shows the diffraction patterns of Zr_{0.005} Ce_{0.005} at different temperatures from room temperature to 140°C at a step of 10°C per scan. Before each of the

$\theta - 2\theta$ scans, the bulk sample was set in isothermal environment until the temperature reading was stable. The temperature sensor was calibrated by the test run of an empty chamber.

The cubic (high temperature phase) and tetragonal (low temperature phase) lattice parameters were refined by $Pm\bar{3}m$ and $P4mm$ space groups by the Rietveld refinement using GSAS suite with EXPGUI [41]. Same procedure was conducted for rest four bulk samples in different compositions. The refined lattice parameters of tetragonal and cubic phases are given in Table S1 (Supplementary information). The as-grown crystal by floating zone method was characterized by synchrotron Laue micro-diffraction in the beamline 12.3.2 at the Advanced Light Source to study the orientation distribution and microstructural property. The focused $1\mu\text{m}$ diameter X-ray beam with energy bandpass 6keV to 22keV was used to conduct Laue microdiffraction scans on several tridoped BT samples cut in different orientations. The X-ray probe scans the surface of polished samples with the area $7.96 \times 4.68 \text{ mm}^2$ for Zr0.005 Ce0.005 slice 1, $19.5 \times 5.5 \text{ mm}^2$ for Zr0.005 Ce0.005 slice 2, and $6.48 \times 4.48 \text{ mm}^2$ for Zr0.01 Ce0.001 slice 2, by step size $5\mu\text{m} \times 5\mu\text{m}$. Fig. 2 in the main texts and Fig. S6(a) in Supplementary information show the Laue patterns and corresponding orientation maps analyzed by XMAS software [42]. Fig. S6(b) compares the polarization – temperature curves between the single crystals Zr0.005 Ce0.005 of different orientations.

Table 1: Summary of energy conversion properties and compatibility of samples developed in this work and important ferroelectrics reported in literature. The $\llbracket P \rrbracket$ is calculated for a 20°C temperature interval near 100°C.

Materials	$\llbracket P \rrbracket$ ($\mu\text{C}/\text{cm}^2$)	κ ($\mu\text{C}/\text{cm}^2\text{K}$)	ℓ (J/cm^3)	FOM ($\mu\text{C}^2/\text{J cm K}$)	Temp. range (°C)
Zr0.005 Ce0.005	7.58	1.31	6.55	1.52	105-125
Zr0.005 Ce0.005 sc	11.68	1.93	6.34	3.55	
Zr0.001 Ce0.005	6.11	1.02	6.20	1.00	105-125
Zr0.01 Ce0.005	5.58	0.54	5.33	0.57	100-120
Zr0.01 Ce0.01	6.48	0.63	5.67	0.72	100-120
Zr0.01 Ce0.001	5.81	0.74	6.53	0.66	105-125
Zr0.01 Ce0.001 coarse	6.27	1.01	6.28	1.01	
BaTiO ₃ sc [16]	6.0	1.0			115-135
Ba(Ti, Zr _{0.017})O ₃ poly[31]	2.5	0.58			120-140
PMN - 0.32PT sc [17]	n.a.	0.08			100-120
PMN - 0.32PT thin film [12]	n.a.	0.055			100-120

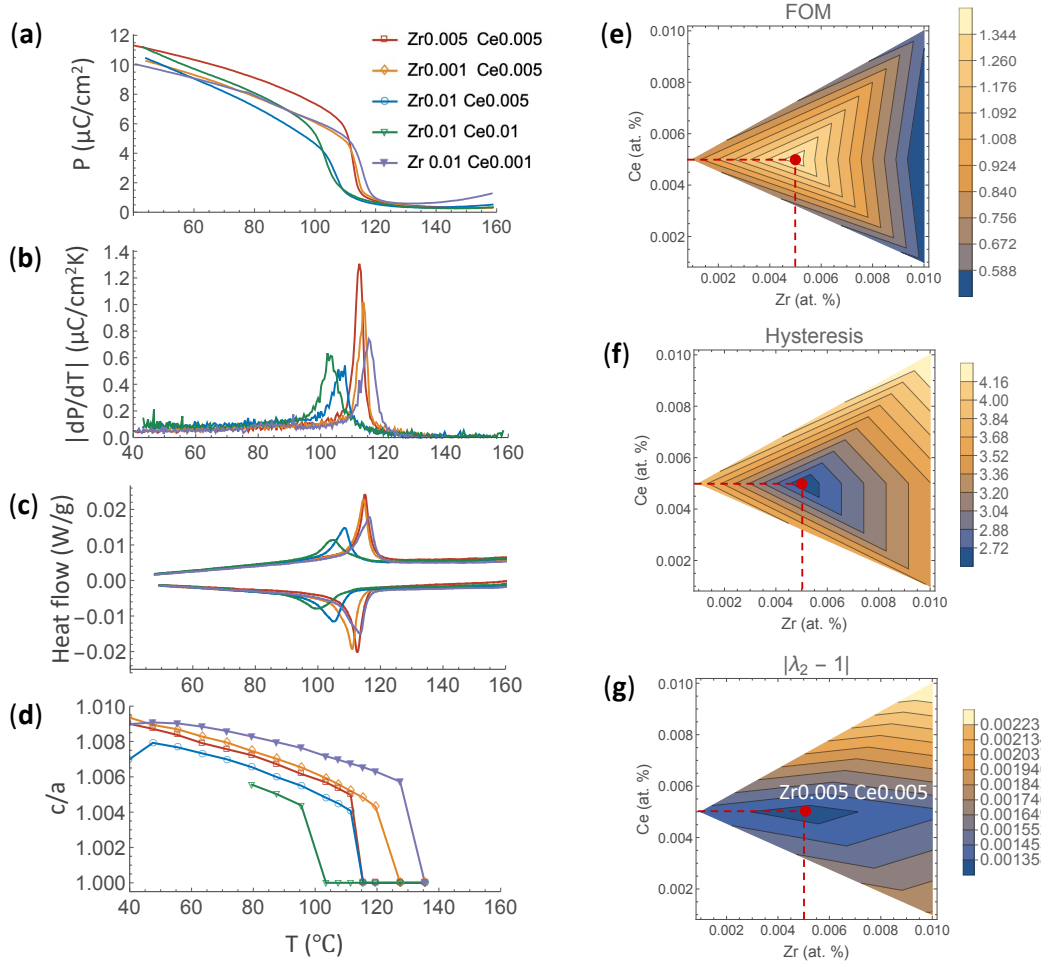


Figure 1: Ferroelectric, thermal and structural characterizations of first-order phase transformation in polycrystalline tridoped BT crystals. (a) and (b) Temperature dependent polarization and absolute value of pyroelectric coefficient dP/dT . (c) Thermal analysis of reversible phase transformations by DSC. (d) Temperature dependent c/a ratio by neutron diffraction experiments. (e)-(g) Contours of FOM, thermal hysteresis and compatibility condition in two dimensional composition space interpreted from experimental data.

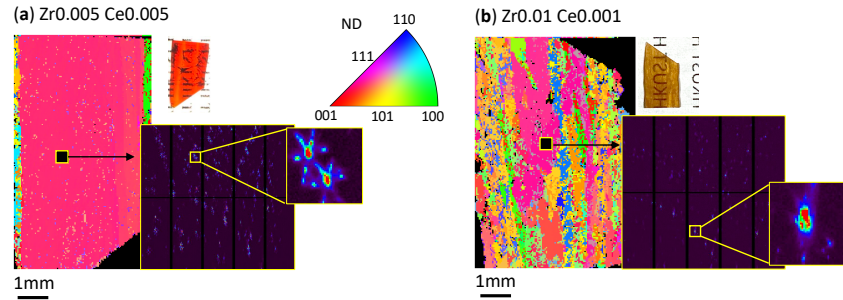


Figure 2: Orientation maps by synchrotron Laue microdiffraction for (a) Zr_{0.005} Ce_{0.005} (b) Zr_{0.01} Ce_{0.001} grown by floating zone method. The color map indicates the orientation of normal direction (ND) of the surface.

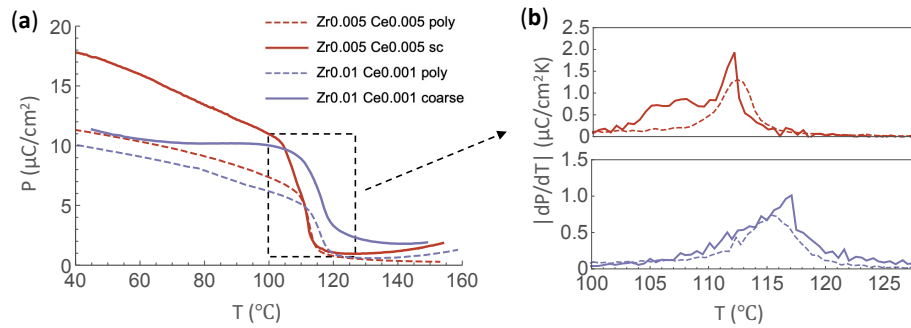


Figure 3: Ferroic properties of Zr_{0.005} Ce_{0.005} single crystal and Zr_{0.01} Ce_{0.001} coarse grain crystal. (a) Temperature dependent polarization and (b) absolute value of dP/dT in a zoomed temperature range between 100 and 130°C.

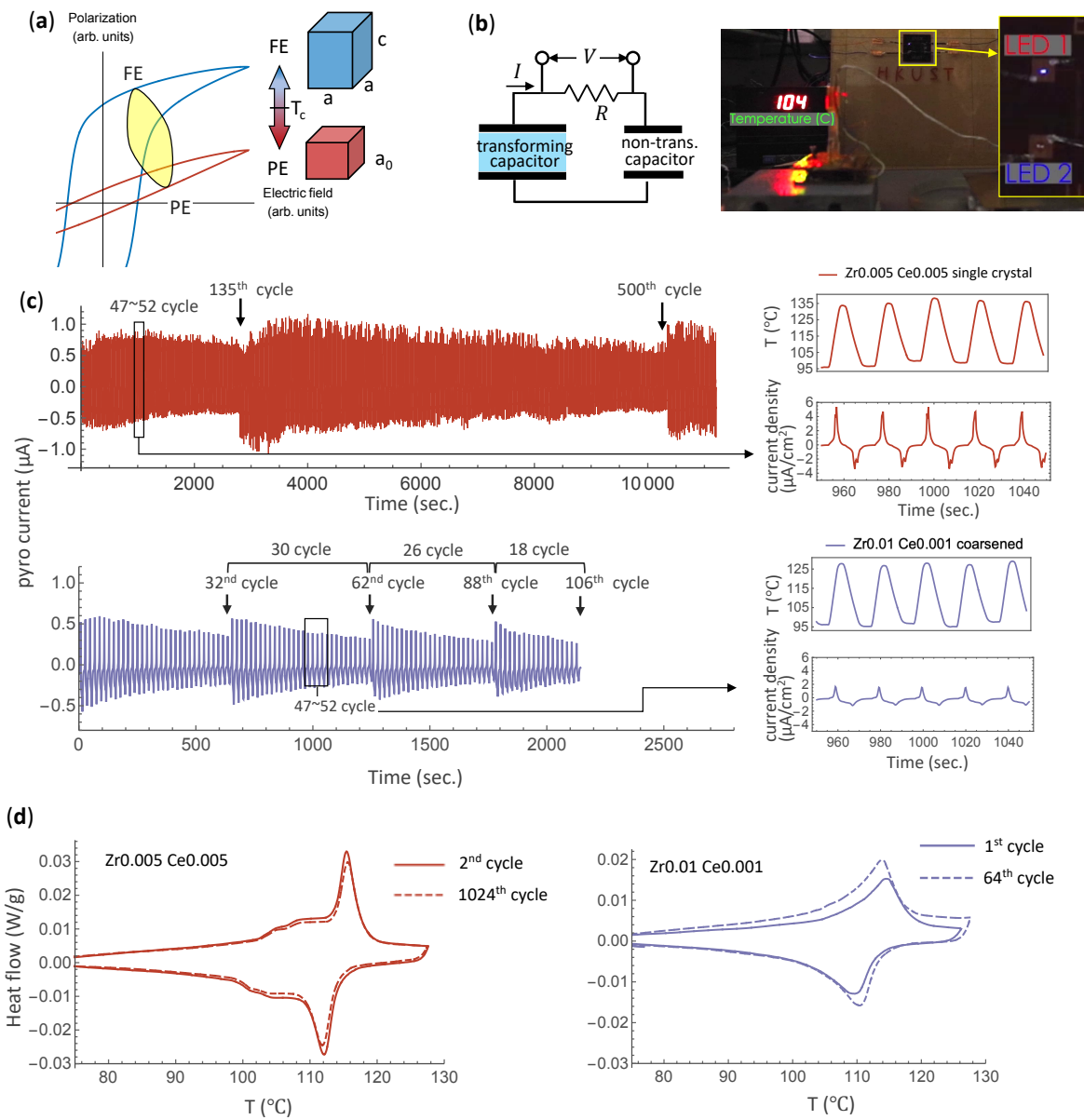


Figure 4: Energy conversion by phase-transforming ferroelectric crystals. (a) Polarization - field curves of tetragonal ferroelectric phase (blue) and cubic paraelectric phase (red). The yellow area demonstrates the thermodynamic cycle of the process without application of external bias electric field. (b) Battery detached setup of the transforming capacitor with polarization jump between ferroelectric and paraelectric phases. The demonstration to light up a LED light during heating. (c) Pyro-current generated by the Zr_{0.005} Ce_{0.005} single crystal capacitor (red) and the Zr_{0.01} Ce_{0.001} coarse-grained capacitor (blue) over hundreds of transformation cycles. The insets are pyroelectric current density of 47 to 52 cycles corresponding to the applied temperature profiles. (d) Differential scanning calorimetry measurement of a Zr_{0.005} Ce_{0.005} single crystal plate (red) and a Zr_{0.01} Ce_{0.001} coarse-grained plate (blue) at initial and late thermal cycles.